PHYSICAL REVIEW A **89**, 053430 (2014)

Experimental and theoretical study of three-photon ionization of He($1s2p\,^3P^o$)

Matthieu Génévriez,[1,*] Xavier Urbain,[1] Mohand Brouri,[1,†] Aodh P. O'Connor,[1,‡]
Kevin M. Dunseath,[2] and Mariko Terao-Dunseath[2]
[1]*Institute of Condensed Matter and Nanosciences, Université catholique de Louvain, Louvain-la-Neuve B-1348, Belgium*
[2]*Institut de Physique de Rennes, UMR 6251 CNRS–Université de Rennes 1, Campus de Beaulieu, F-35042 Rennes cedex, France*

(Received 21 March 2014; published 30 May 2014)

A joint experimental and theoretical study of three-photon ionization of the $1s2p\,^3P^o(M_L = 0,\pm1)$ states of helium is presented. The ion yield is recorded in the 690–730 nm wavelength range for different laser pulse energies, using an excited helium beam produced by photodetachment of helium negative ions. Two series of asymmetric peaks due to two-photon resonances with $1snp$ and $1snf$ Rydberg states are observed. In one series, the peaks have tails towards higher frequencies, while in the other series the tails change direction for higher Rydberg states. An effective Hamiltonian is built in the dressed state picture, and a numerical model simulating the traversal of the helium atom across the laser pulse is developed. The simulated and observed ion yields are in good qualitative agreement. The observed behavior is shown to result from the contributions of two different resonantly enhanced multiphoton ionization processes, depending on the magnetic quantum number M_L of the initial state. The asymmetry reversal is explained by the strong $1s2p$–$1s3s$ dynamic Stark mixing for $M_L = 0$.

DOI: 10.1103/PhysRevA.89.053430 PACS number(s): 32.80.Rm, 32.80.Gc, 31.10.+z, 37.20.+j

I. INTRODUCTION

Helium is the second simplest—albeit not simple—atomic system and is, in this respect, a perfect candidate for the study of correlation in photon-atom interactions. Photoionization from the ground state has been extensively studied and is today very well understood both theoretically and experimentally [1]. Over the past few decades, attention has focused on double photoionization of the ground state and autoionization from doubly excited states [2–4]. Little is known, however, concerning the photoionization of excited states. Early experiments by Stebbings *et al.* [5] gave a first account of the photoionization cross sections from the $1s2s\,^{1,3}S$ states, along with theoretical work by, for example, Burgess and Seaton [6] and by Jacobs [7]. Later, Gisselbrecht *et al.* [8] used high-harmonic generation techniques to measure photoionization cross sections of the $1s2p$ and $1s3p$ singlet states, obtaining satisfactory agreement with theoretical work by Chang and Zhen [9] and Chang and Fang [10].

Data concerning *multiphoton* ionization (MPI) of excited states of helium are even scarcer. In 1974, Dunning and Stebbings [11] used a two-photon ionization scheme, but focused on the determination of single-photon ionization cross sections of $^3P^o$ states. Lompré *et al.* [12] investigated two-photon ionization of the $1s2s\,^{1,3}S$ excited states of helium for two wavelengths, a phenomenon Haberland *et al.* [13] also considered in a narrow wavelength region around 500 nm where the process is resonantly enhanced. More recently, Madine and van der Hart [14,15] used R-matrix Floquet theory (RMF) to examine the competition between multiphoton ionization of inner and outer shell electrons of the $1s2s\,^1S$ and $1s3s\,^1S$ states of helium in a VUV radiation field.

The present article describes a joint experimental and theoretical study of three-photon ionization of the $1s2p\,^3P^o$ state of helium, for laser wavelengths in the range 690–730 nm and pulse peak intensities of the order of 10^{10} W/cm^2 in the beam focus. Compared to previous studies, the larger number of photons exchanged, combined with a wider range of laser field intensities and frequencies, is expected to induce a complex interplay of low-lying excited states and Rydberg states, as shown schematically in Fig. 1.

In the range of wavelengths considered here, a helium atom in the $1s2p\,^3P^o$ state must absorb at least three photons to ionize. It is well known that ionization efficiency can be enhanced by intermediate resonant states, e.g., one of the many high-lying $1snp$ and $1snf$ states that can be reached by two-photon absorption. Absorption of one further photon leads to the emission of an electron in the $\ell = 0,2,4$ continua, and the whole process may be described as following a $(2+1)$ REMPI (resonance-enhanced multiphoton ionization) scheme. Figure 1 also reveals the existence of another possible REMPI scheme: For $\lambda \approx 706.7$ nm, the photon energy $\omega \approx 0.064\,47$ a.u. coincides with the energy difference between the field-free He($1s2p\,^3P^o$) and He($1s3s\,^3S$) states. The latter is in one-photon resonance with the $1s11p$ state which can emit a photoelectron in the $\ell = 0,2$ continua by absorbing one further photon. Such a $(1+1+1)$ REMPI scheme is rare in atomic multiphoton ionization since the most studied initial state, the ground state, is far below the excited states. The presence of two intermediate resonance states instead of only one significantly enriches the ionization behavior. The competition between the two REMPI schemes is also interesting as their behavior depends on the magnetic quantum number M_L of the initial state $1s2p\,^3P^o$. For $M_L = \pm1$, only the well-known $(2+1)$ scheme is allowed, while for $M_L = 0$, the $(1+1+1)$ process is also permitted. We have found that this difference induces a very unusual behavior in the MPI rates as a function of the laser wavelength, which extends quite far from the resonance between the field-free He($1s2p\,^3P^o$) and He($1s3s\,^3S$) states due to their one-photon dynamic Stark mixing.

---

[*] matthieu.generiez@uclouvain.be

[†] Present address: Lam Research, 75 Kapeldreef, B3001 Leuven, Belgium.

[‡] Present address: Max-Planck-Institut für Kernphysik, Saupfercheckweg 1 D-69117 Heidelberg, Germany.

1050-2947/2014/89(5)/053430(11)

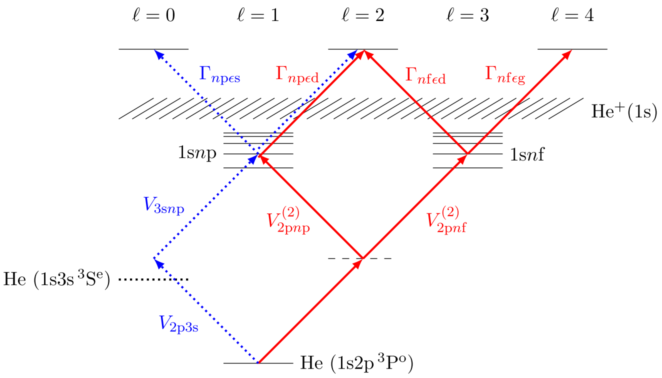

FIG. 1. (Color online) Schematic energy level diagram. The dotted arrows correspond to $(1+1+1)$ REMPI, allowed only for $M_L = 0$, while the full arrows represent a $(2+1)$ REMPI, allowed for both $M_L = 0$ and $M_L = \pm 1$. The interactions $V_{ij}^{(2)}$ are two-photon dipole matrix elements, while $\Gamma_{i\varepsilon\ell}$ are partial ionization rates.

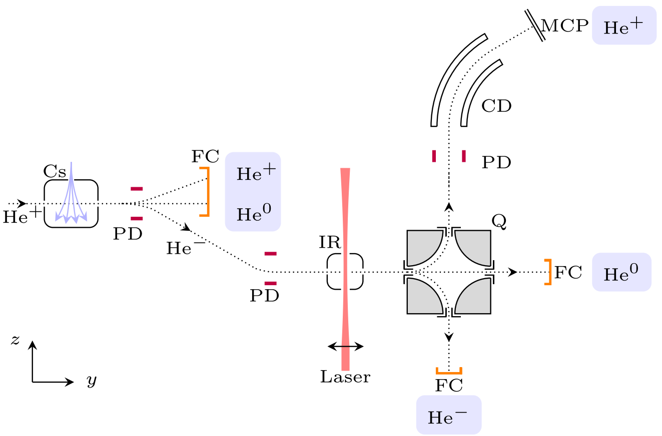

FIG. 2. (Color online) Experimental setup. Cs: cesium vapor cell; PD: planar deflector; FC: Faraday cup; CD: cylindrical deflector; IR: interaction region; Q: quadrupolar deflector; MCP: multichannel plates. The double arrow indicates a convergent lens. The laser beam propagates along the z direction and its polarization is along the y axis.

The structure of the paper is as follows: Details of the experiment are presented in Sec. II; the effective Hamiltonian approach together with the R-matrix Floquet and the Coulomb discrete variable representation (DVR) methods used to calculate field-dressed quasienergies and two-photon dipole transition matrix elements are summarized in Sec. III; details of the model developed to simulate the system over a wide range of laser intensities and wavelengths are presented in Sec. IV; results of the numerical simulations and comparison with experimental data are discussed in Sec. V. Atomic units ($\hbar = 1$, $e = 1$, $m_e = 1$) are used unless otherwise stated.

II. EXPERIMENTAL SETUP

The production of He($1s2p$) in a triplet state is experimentally challenging as it is forbidden by optical dipole excitation from the ground state. Previous experiments [13,16] have shown that both singlet and triplet metastable states are present in gas discharges. Photodetachment of the helium negative ion He$^-$($1s2s2p\ ^4P^o$), however, offers the possibility of overcoming this difficulty as the resulting neutral helium atoms are left in the $1s2s\ ^3S$ and $1s2p\ ^3P^o$ states, whose energies are easily resolved in subsequent photoionization experiments. Its relatively long lifetime ($\tau \sim 365\ \mu$s for the $J = 5/2$ component [17]) furthermore allows conventional beam transport and detection techniques to be applied. The main difficulty of the experiment thus lies in producing He$^-$ in sufficiently large quantities. Regular ion sources cannot be used since the binding energy of this negative ion is very weak, 77.52 meV [17]. It can, however, be produced from He$^+$ by double electron capture on alkali-metal atoms. The first stage of the experimental setup, sketched in Fig. 2, comprises a duoplasmatron source providing a 4 keV He$^+$ beam which is passed through a cesium vapor cell, where charge transfer converts it into He($1s2s\ ^{1,3}S$) and He$^-$($1s2s2p\ ^4P^o$). The production of He$^-$ requires a large target density for multiple collisions to occur, resulting in a conversion efficiency around 1%. After passing the vapor cell, a double deflection, using electrostatic plates, subsequently cleans the beam of its neutral and positive components. The remaining He$^-$ beam is passed into the laser interaction region which is pumped to a high vacuum of about 10^{-8} mbar. Contamination of the ion beam by neutrals at the percent level still occurs due to spontaneous detachment of the $J = 1/2$ and $J = 3/2$ states to the ground state with a lifetime of the order of 11 μs [18].

The 1 mm ion beam is illuminated perpendicularly by nanosecond pulses from a tunable dye laser pumped by the second harmonic of a Nd:YAG laser. The dye laser is operated using pyridine 1 and 2 dyes, in order to scan the 690–730 nm wavelength range. A pyroelectric detector constantly monitors the pulse energy, which can be attenuated using a combination of a rotating half-wave plate and a polarizing beam-splitter cube placed at the output of the dye laser. The $\lambda/2$-plate is servo controlled by the detector to ensure a constant pulse energy along the dye gain curve. The laser beam is focused down to a 54 μm waist, resulting in a peak intensity of 3.9×10^{10} W/cm^2 for 8 mJ pulses. Ions traverse the laser spot (twice the waist) in about 250 ps, which is much shorter than the pulse duration whose full width at half maximum is 4.84 ns. The measured signal is hence averaged over the focal volume and integrated over the pulse duration. It must be noted that two successive events occur within the interaction volume: the photodetachment of He$^-$($1s2s2p\ ^4P^o$), leaving neutral He in either the $1s2s\ ^3S$ or the $1s2p\ ^3P^o$ state, and the three-photon ionization of He($1s2p\ ^3P^o$). Within the experimental wavelength range, the ionization of the $1s2s\ ^3S$ state proceeds through the nonresonant absorption of three photons and is thus expected to give a negligible contribution to the measured signal.

Subsequent energy analysis of He$^+$ ions by a quadrupolar deflector [19] coupled with a 60° cylindrical deflector ensures the selection of laser-induced double ionization events, while negative ions are collected at the opposite side of the quadrupole in a Faraday cup. In addition to the energy analysis, a temporal gating of the 60° deflection and the signal acquisition is performed: The cylindrical deflector is switched on only during a narrow time window centered around the time of flight of laser-produced He$^+$, whose hits on the multichannel plates are subsequently recorded in coincidence with a square signal of a few tens of nanoseconds, appropriately delayed with respect to the laser pulse. The energy selection and temporal gating reduce the background to less than three counts per hundred laser shots, as determined in a shifted time window of the same duration.

The use of multichannel plates allows the detection of single ions. As a result of this extreme sensitivity, however, it is not possible to distinguish between single and multiple ion formation within the same laser shot. A correction must be applied to the measured rate to account for the Poisson probability distribution of multiple ionization events

$$N_{\mathrm{corr}} = -N_p \ln(1 - N_{\mathrm{meas}}/N_p), \tag{1}$$

where N_{meas} (N_{corr}) is the measured (corrected) number of events recorded after N_p laser pulses. The corrected results are further normalized by the measured He$^-$ current.

In the spectra presented below, the ionization yield at each wavelength is recorded over 1000 laser pulses. The overall uncertainty is of the order of 5%–10% and is dominated by counting statistics with small contributions from the pulse energy readout and variations in the laser pulse shape.

III. THEORY

A. *R*-matrix Floquet theory

R-matrix Floquet theory [20,21] allows atomic processes in a laser field to be described in an *ab initio* and nonperturbative way. The theory has been successfully applied to the investigation of MPI, laser-assisted scattering, harmonic generation, and laser-induced continuum states. Details of the theory together with particularly illustrative examples of its application can be found in the recent books [3,22]. Here, only those features that are relevant to the current study will be outlined.

The wave function of an $(N+1)$-electron system in a linearly polarized laser field described in the dipole approximation by the vector potential $A_0\hat{\boldsymbol{\epsilon}}\cos\omega t$ can be expressed in terms of a Floquet-Fourier expansion

$$\Psi(\boldsymbol{X}_{N+1},t) = e^{-iEt}\sum_{n=-\infty}^{\infty} e^{-in\omega t}\Psi_n(\boldsymbol{X}_{N+1}), \tag{2}$$

where $\boldsymbol{X}_{N+1}$ is the set of space and spin coordinates of all $N+1$ electrons. Inserting (2) into the time-dependent Schrödinger equation

$$i\frac{\partial}{\partial t}\Psi(\boldsymbol{X}_{N+1},t) = \left[H_{N+1} - \frac{i}{c}\boldsymbol{A}(t)\cdot\sum_{e=1}^{N+1}\nabla_e + \frac{N+1}{2c^2}\boldsymbol{A}^2(t)\right]\Psi(\boldsymbol{X}_{N+1},t)$$

yields an infinite set of time-independent coupled equations for the Floquet components $\Psi_n(\boldsymbol{X}_{N+1})$. These equations can be solved efficiently using the *R*-matrix approach of partitioning configuration space into subregions with locally adapted gauges and reference frames.

The inner region is defined as the sphere of radius a encompassing the N-electron states $\Phi_i(\boldsymbol{X}_N)$ retained in the calculation to describe the residual ion. The components $\Psi_n(\boldsymbol{X}_{N+1})$ are expanded in a basis of fully antisymmetrized wave functions built from $\Phi_i(\boldsymbol{X}_N)$ and continuum orbitals $u_{n\ell}$ satisfying a fixed logarithmic boundary condition at $r=a$. The most appropriate gauge to use in this region is the length gauge, in which the interaction of the atomic system with the laser field is proportional to the distance of the electrons from the nucleus. The corresponding Hamiltonian is diagonalized in the Floquet $(N+1)$-electron basis. The amplitudes of the eigenvectors at $r=a$ and the eigenvalues are used to calculate the *R*-matrix elements, i.e., the inverse of the logarithmic derivatives in the reaction channels.

In the outer region, the photoelectron moves far from the nucleus while the other electrons remain bound. Since the radiative interaction in the length gauge diverges at large distances, a transformation to the velocity gauge is performed on the photoelectron, while the interaction of the field with the other electrons is still described in the length gauge. In the outer region, exchange of the photoelectron with the remaining bound electrons is negligible so that (2) reduces to an infinite set of ordinary differential equations that can be solved using a close-coupling approach combined with a log-derivative propagation method. At sufficiently large distances, the solutions are matched to Siegert outgoing boundary conditions defined in the acceleration frame where the close-coupling equations are asymptotically uncoupled and propagated inwards using an asymptotic expansion technique. The matching is possible only at particular complex quasienergies E, whose real part gives the Stark-shifted energy of the dressed atomic states and whose imaginary part is minus half the dressed state ionization rate. The quasienergies for each state are found by an iterative search in the complex energy plane, usually starting from the zero-field values, and followed adiabatically as the laser frequency or intensity changes. Near resonance, this can require very small steps and hence a very large number of individual calculations. This is also true when the imaginary part of the state being followed is extremely small, for example, the $1s2p$ state.

As the photon energy is relatively small, the residual He$^+$ ion can be assumed to be left in its ground state. Since the initial state is He($1s2p\ {}^3P^o$), the set of N-electron states $\Phi_i(\boldsymbol{X}_N)$ is limited to He$^+(1s)$. Due to this approximation, the ionization potentials of He($1s2p\ {}^3P^o$) and He($1s3s\ {}^3S$), respectively 3.5333 and 1.8637 eV, are underestimated by 0.05 and 0.005 eV. The radius of the inner region was taken to be $6a_0$. Seven Floquet components (five absorption and one emission) were retained in expansion (2), together with angular momenta ℓ up to 11. The inner region solutions were propagated to $65a_0$ where they were matched to outgoing Siegert boundary conditions.

The real parts of the quasienergies obtained are shown in Fig. 3 for $M_L=\pm1$ and Fig. 4 for $M_L=0$ as a function of the photon energy ω. In Fig. 3, the horizontal line corresponds to the energy of the He($1s2p\ {}^3P^o$) state, while the slanted lines correspond to the energy of the Rydberg He($1snp$) and He($1snf$) states dressed by two photons. Figure 4 also includes the He($1s3s\ {}^3S$) state dressed by one photon. A detailed explanation of these figures will be given in Sec. V, but one can already see major differences between the $M_L=\pm1$ and $M_L=0$ cases, hinting at different physical behaviors depending on the value of the magnetic quantum

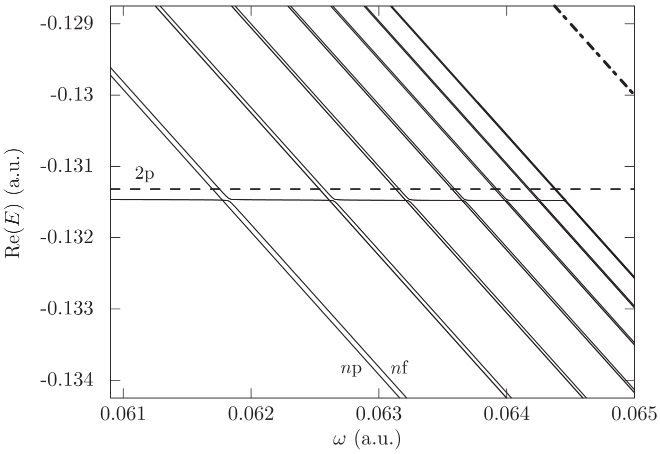

FIG. 3. Real part of the RMF quasienergies for $M_L = \pm 1$ and dressed Rydberg states from $n = 8$ to $n = 14$, as a function of the laser angular frequency at a fixed intensity of 3.6×10^{10} W/cm^2. The dashed line indicates the zero-field energy of the $1s2p$ state and the thick dot-dashed line in the upper right corner is the two-photon ionization threshold.

number. For $M_L = 0$, the presence of the $1s3s$ state dressed by one photon gives rise to a very large avoided crossing around $\omega_r = 0.062\,82$ a.u. between the $1s2p$ and $1s3s$ energy curves, reflecting the strong interaction between these two states, which is absent in the $M_L = \pm 1$ case. The energy of He($1s2p\ {}^3P^o$) is shifted down for $\omega < \omega_r$ and up for $\omega > \omega_r$, in contrast to the $M_L = \pm 1$ case where the energy is always shifted down. The Stark shift of the Rydberg states (present as a series of lines with slope -2ω) is negligible.

The RMF calculation corresponds to a well-defined intensity but a simple time-dependent picture can be built using a naive two-state model involving the strongly interacting $1s2p$ and $1s3s$ states. This is justified by the observation that in the RMF calculation the Rydberg states are not appreciably perturbed by the field. The field-dressed wave functions can be written as

$$|\psi_+(t)\rangle = \sin\theta(t)|2p\rangle + \cos\theta(t)|3s\rangle, \tag{3}$$

$$|\psi_-(t)\rangle = \cos\theta(t)|2p\rangle - \sin\theta(t)|3s\rangle, \tag{4}$$

with

$$\theta(t) = \frac{1}{2}\arctan\left(\frac{\Omega(t)}{\Delta}\right), \quad 0 \leqslant \theta(t) \leqslant \pi/2. \tag{5}$$

The detuning Δ is defined by $\Delta = E_{3s} - \omega - E_{2p}$, while $\Omega(t)$ is the Rabi frequency

$$\Omega = \mathscr{E}_0(t)\langle 3s|\hat{\boldsymbol{\epsilon}} \cdot \boldsymbol{r}|2p\rangle \tag{6}$$

with $\mathscr{E}_0(t)$ the amplitude of the electric field at time t, $\hat{\boldsymbol{\epsilon}}$ the polarization vector, and $\boldsymbol{r}$ the radial coordinate of the electron. Defining $E_0 = (E_{3s} - \omega + E_{2p})/2$, the energies of the two states are given by

$$E_\pm = E_0 \pm \tfrac{1}{2}\sqrt{\Omega^2(t) + \Delta^2} \tag{7}$$

which tend to $E_0 \pm |\Delta|/2$ as the electric field and hence $\Omega(t)$ tends to zero.

We first consider $\Delta > 0$, corresponding to photon energies below the $1s2p$-$1s3s$ resonance. For vanishing fields, θ tends to 0 and the $1s2p$ state corresponds to $|\psi_-\rangle$, while the $1s3s$ state corresponds to $|\psi_+\rangle$. As the electric field increases, the energy of the $1s2p$ evolves adiabatically as E_-, i.e., is shifted down with respect to the field-free energy. As the Rydberg states are not appreciably perturbed by the field, this results in a blueshift of the $1s2p$-$1snp$ resonances. When the photon energy is above the $1s2p$-$1s3s$ resonance, we have $\Delta < 0$ and hence $\theta = \pi/2$ for vanishing fields. The $1s2p$ state thus corresponds to $|\psi_+\rangle$ and its energy evolves adiabatically as E_+, inducing a red-shift in the resonance positions.

This naive approach provides some insight on the mechanisms taking place in the ionization process under study. In particular, the sign of the shift is determined uniquely by the laser frequency ω, while its amplitude varies in time following $\mathscr{E}_0(t)$. The change from blueshift to redshift is expected to leave a strong signature in the experimental ionization spectra, along with major differences between the $M_L = 0$ and $M_L = \pm 1$ cases.

The next section is dedicated to a more realistic model of the experiment.

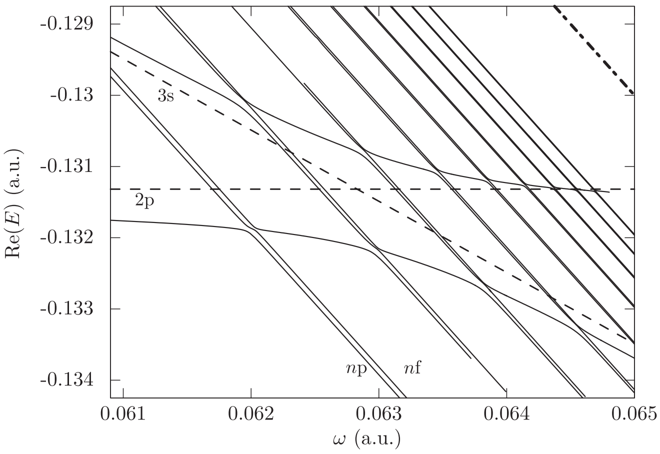

FIG. 4. Real parts of the RMF quasienergies for $M_L = 0$ and dressed Rydberg states from $n = 8$ to $n = 16$, as a function of the laser angular frequency at a fixed intensity of 3.6×10^{10} W/cm^2. The horizontal dashed line indicates the zero-field energy of the $1s2p$ state, while the oblique dashed line represents the zero-field energy of the $1s3s$ state shifted down by ω. The thick dot-dashed line in the upper right corner is the two-photon ionization threshold.

B. Effective Hamiltonian approach

The RMF theory is a powerful tool for studying multiphoton ionization of complex atoms but may require lengthy computation, especially close to resonance. It is therefore not adapted to a detailed modeling of an actual experiment where ionization rates over a large range of laser intensities are required. A more practical and versatile approach is provided by effective Hamiltonian (EH) theory [23], whose scope goes well beyond atom-laser interactions, as shown in the comprehensive reviews by Killingbeck and Jolicard [24,25].

The underlying idea of EH theory is twofold. First, the Hilbert space is partitioned into two different subspaces: the *model* space $\mathscr{P}$, containing the most relevant states of the problem, which in our case are the quasiresonant bound states, and its orthogonal complement $\mathcal{Q}$, spanning the rest of the Hilbert space. Second, the exact Hamiltonian is "folded" into a smaller, effective Hamiltonian which couples explicitly only those states belonging to the model space. The effect of states in the $\mathcal{Q}$ space is treated through additional perturbative matrix elements, illustrating the *semiperturbative* nature of the EH approach. The choice of which states to include in the model space is of critical importance as the effective Hamiltonian aims to preserve the main physical properties of the process under study while treating perturbatively or even omitting the remaining states.

In the current case the $\mathcal{P}$ space includes the $1s2p\ ^3P^o$, $1s3s\ ^3S$, $1s3d\ ^3D$, $1snp\ ^3P^o$, and $1snf\ ^3F^o$ states, with n spanning the range 4–25, leading to an effective Hamiltonian of dimension 47. The $\mathcal{Q}$ space is truncated to a finite size and includes ^3S, ^3D, and ^3G states together with high-lying $^3P^o$ and $^3F^o$ states with $n = 26$–30, sufficient to ensure convergence. Continuum states are included up to energies where bound-free couplings are negligible. The energy of the $1s2p\ ^3P^o$, $1s3s\ ^3S$, and $1s3d\ ^3D$ states, respectively $-0.133\,154$, $-0.068\,681\,6$, and $-0.055\,628\,8$ a.u. are taken from the NIST database [26], while the energy of the Rydberg states is calculated using quantum defects given by Drake [27].

The effective Hamiltonian H_{eff} gives rise to the following eigenvalue equation:

$$H_{\text{eff}}|\psi_p\rangle = E|\psi_p\rangle, \tag{8}$$

where the wave function $|\psi_p\rangle$ spans the model space and the complex eigenvalue E has a real part ideally identical to an eigenvalue of the exact Hamiltonian. A complete and rigorous derivation of general effective Hamiltonians has been given by Durand [28], while the application of EH theory to REMPI is described by Baker [23]. The effective Hamiltonian, valid up to the second order in the atom-field interaction, is written as

$$H_{\text{eff}} = PH_0P + PVP + P\left(S + \Omega - i\frac{\Gamma}{2}\right)P, \tag{9}$$

where V is the exact atom-field interaction operator and H_0 is the exact "free" Hamiltonian, containing the field-free atomic Hamiltonian and the light-field Hamiltonian. The eigenvalues of the bound states of H_0 will be denoted by $E_i = \mathcal{E}_i - m\omega$, where $\mathcal{E}_i$ is the energy of the field-free bound states and m is the number of photons absorbed. By convention, m is 0 for $1s2p\ ^3P^o$, 1 for $1s3s\ ^3S$ and $1s3d\ ^3D$, and 2 for the Rydberg states in the model space. The eigenvalues of the continuum states of H_0 are, similarly, $e = \varepsilon - 3\omega$, where ε is the photoelectron energy. P is the Feshbach projection operator, projecting the wave function onto the $\mathcal{P}$ space:

$$P = \sum_{i\in\mathcal{P}} |i\rangle\langle i|. \tag{10}$$

The operators S, Ω, and Γ are perturbations of the states in the model space due to those in $\mathcal{Q}$ space. Their physical significance is standard in second-order perturbation theory: S and Ω are two-photon transition operators connecting quasiresonant bound states via, respectively, the nonresonant bound states and the ionization continuum states ($\mathcal{Q}$ space), while Γ is the ionization width of the model space states. They are given by

$$S = \sum_{k\in\mathcal{Q}} \frac{V|k\rangle\langle k|V}{E_i - E_k}, \tag{11}$$

$$\Omega = \mathrm{P}\int de \frac{V|e\rangle\langle e|V}{E_i - e}, \tag{12}$$

$$\Gamma = 2\pi\ V|e\rangle\langle e|V|_{e=E_i}, \tag{13}$$

where $|e\rangle$ is an ionization continuum state, identified by the photoelectron energy ε, its angular momentum ℓ, and magnetic quantum number m_ℓ. Similarly, $|k\rangle$ is a bound state in $\mathcal{Q}$ space identified by the principal, angular, and magnetic quantum numbers n, ℓ, and m_ℓ. $\mathrm{P}\int$ represents a Cauchy principal value integration.

In practice, the calculation of the various elements of H_{eff} is performed within the dipole and rotating-wave approximations [29], justified by the moderate laser intensities involved and the treatment of only quasiresonant bound states. The interaction of the jth electron with the laser field is given by the dipole moment operator $\hat{\boldsymbol{\epsilon}} \cdot \boldsymbol{r}_j$, with $\hat{\boldsymbol{\epsilon}}$ the polarization vector and $\boldsymbol{r}_j$ the radial coordinate of the electron.

The two-photon dipole matrix elements between the $1s2p$ and $1sn\ell$ bound states are calculated using perturbation theory:

$$V^{(2)}_{2pn\ell} = \frac{\mathcal{E}_0^2}{4}\sum_k \frac{\langle 1sn\ell|\ \hat{\boldsymbol{\epsilon}}\cdot\boldsymbol{R}\ |k\rangle\langle k|\ \hat{\boldsymbol{\epsilon}}\cdot\boldsymbol{R}\ |1s2p\rangle}{\mathcal{E}_{1s2p} + \omega - \mathcal{E}_k}, \tag{14}$$

where $\mathcal{E}_0$ is the amplitude of the electric field, $\boldsymbol{R} = \boldsymbol{r}_1 + \boldsymbol{r}_2$, and the sum is over all intermediate bound and continuum states coupled to the initial and final states. The one-photon dipole matrix elements appearing in Eq. (14) are obtained from a two-electron Coulomb DVR [30] calculation which is able to furnish accurate energies for a large number of states, as well as their oscillator strengths. In this method, the two-electron wave functions are expanded in a basis of antisymmetrized linear combinations of the product of two one-electron DVR basis functions, themselves constructed from zeros of a reference Coulomb function. Diagonalizing the two-electron Hamiltonian in this basis yields a set of energies and wave functions, of which the lowest correspond to the physical bound states, while the others are pseudostates representing higher-lying excited states and the continuum. The infinite sum appearing in Eq. (14) is then replaced by a finite sum over these states and pseudostates.

The dipole moments connecting Rydberg and continuum states are calculated using quantum defect theory (QDT) [31]. Their angular parts are given by straightforward angular momentum algebra, whereas their radial parts

$$\int_0^\infty dr\ R^*_{\varepsilon\ell}(r) r^3 R_{\bar{n}\ell}(r) \tag{15}$$

are obtained by numerical integration of the bound and continuum QDT radial wave functions:

$$rR_{\bar{n}\ell}(r) = K(\bar{n},\ell)W_{\bar{n},\ell+1/2}(2r/\bar{n}), \tag{16}$$

$$rR_{\varepsilon\ell}(r) = s(\varepsilon,\ell;r)\cos[\pi\delta_\ell(\varepsilon)] + c(\varepsilon,\ell;r)\sin[\pi\delta_\ell(\varepsilon)], \tag{17}$$

where $\delta_\ell(\varepsilon)$ is the quantum defect extrapolated to positive photoelectron energy ε; $s(\varepsilon,\ell;r)$ and $c(\varepsilon,\ell;r)$ are the normalized regular and irregular Coulomb functions [32]; $K(\bar{n},\ell)$ is a normalization factor [31]; and $W_{\bar{n},\ell+1/2}(2r/\bar{n})$ is a Whittaker function. In order to avoid divergence at $r = 0$, the irregular Coulomb and Whittaker functions are also multiplied by a cut-off factor $[1 - \exp(-\tau_\ell r)]^{2\ell+1}$ [6]. In QDT, the effective principal quantum number $\bar{n}$ is given by the difference of the principal quantum number n and the associated quantum defect $\delta_\ell(n)$. The values used here are calculated from Ritz's expansion with coefficients taken from Drake [27]. Coulomb and Whittaker functions are calculated using the routines by Barnett [33] and Noble [34], respectively, while quadratures are performed with the standard QUADPACK routines [35] requesting a 10^{-6} relative accuracy. We have verified that this numerical approach allows the fast generation of bound-free dipole moments for photoelectron energies ranging from 0 to a few a.u. and Rydberg bound states up to $n = 98$, the limit of the Whittaker function routine.

It is then straightforward to obtain the numerical values of the two-photon matrix elements

$$\Gamma_{ij} = \frac{\pi \mathcal{E}_0^2}{2} \langle j|\hat{\boldsymbol{\epsilon}} \cdot \boldsymbol{r}|e\rangle\langle e|\hat{\boldsymbol{\epsilon}} \cdot \boldsymbol{r}|i\rangle\bigg|_{e=E_i} \qquad (18)$$

from the one-photon dipole matrix elements. The matrix element

$$\Omega_{ij} = \frac{\mathcal{E}_0^2}{4} \, \mathrm{P}\!\int de \frac{\langle j|\hat{\boldsymbol{\epsilon}} \cdot \boldsymbol{r}|e\rangle\langle e|\hat{\boldsymbol{\epsilon}} \cdot \boldsymbol{r}|i\rangle}{E_i - e} \qquad (19)$$

requires an additional Cauchy principal value integration, performed numerically. The computational costs can be reduced by making extensive use of the $\bar{n}^{-3/2}$ scaling of single-photon bound-bound and bound-free dipole moments.

IV. MODELING

The experimental process is, of course, time dependent, hence its modeling must set the static EH picture developed above "in motion." The helium atom traveling through the laser pulse experiences a time-varying intensity envelope $I(t)$. Hence the quantities V, Ω, Γ, and S in the EH theory also vary, V being proportional to $\sqrt{I(t)}$ and S, Ω, and Γ to $I(t)$. Up to second order in perturbation theory, the effective Hamiltonian H_{eff} derived from the time-independent eigenvalue equation also satisfies the time-dependent Schrödinger equation:

$$i\frac{d|\psi_p(t)\rangle}{dt} = H_{\text{eff}}(t)|\psi_p(t)\rangle \qquad (20)$$

as shown by, e.g., Baker [23]. A formal solution may then be written as

$$|\psi_p(t + \Delta t)\rangle = e^{-iH_{\text{eff}}(t)\Delta t}|\psi_p(t)\rangle. \qquad (21)$$

The wave function is propagated in time up to about 4×10^7 a.u. in steps of $\Delta t \leqslant 10^4$ a.u., by numerically approximating the matrix exponential $e^{-iH\Delta t}$ using routines from EXPOKIT [36]. The model space wave function is given by

$$\begin{aligned} |\psi_p(t)\rangle = {} & c_{2p}(t)|2p\rangle + c_{3s}(t)|3s\rangle + c_{3d}|3d\rangle \\ & + \sum_n (c_{np}|np\rangle + c_{nf}|nf\rangle), \end{aligned} \qquad (22)$$

where the $1s$ orbital has been omitted from the notation for simplicity. The initial condition is obviously $c_{2p}(t = 0) = 1$, while all other coefficients are zero. Although the wave function is initially normalized to unity, its norm may decrease with time due to the non-Hermiticity of H_{eff}. This loss of normalization corresponds to an outgoing flux of electrons and its value after the propagation is the ionization probability P_{He^+}. The values of the coefficients $c_{n\ell}$ at a particular time t provide the instantaneous electronic population of the diabatic bound states.

In the experiment, the laser operates near the TEM$_{00}$ mode, with a Gaussian spatial profile. The time profile of the pulse, $g(t_p)$, has been measured by a fast photodiode and its analytic fit, used in the modeling, is given by the piecewise function

$$g(t_p) = \begin{cases} \cos^2\left(\pi \frac{t_p}{7.81}\right) & \text{if } 0 > t_p \geqslant -3.9, \\ e^{-(t_p/2.29)^2} & \text{if } t_p \geqslant 0, \\ 0 & \text{otherwise}, \end{cases} \qquad (23)$$

where t_p is in nanoseconds. This profile has a full width at half maximum of 4.84 ns. The confocal parameter of 2.62 cm, large compared to the diameter of the atomic beam, allows the waist size w_0 to be taken as constant across the atomic beam. The intensity profile is thus given by

$$I(t;x,t_p) \simeq I_0 \, g(t_p + t) \, e^{-2[x^2+(v_{\text{He}}t)^2]/w_0^2}, \qquad (24)$$

where I_0 is the peak intensity of the pulse, t the travel time through the laser beam, and v_{He} the velocity of the atom. The x direction is perpendicular to the direction of both the laser and atomic beams. The parameter t_p refers to the point on the pulse envelope experienced by the atom when at the center of the laser beam ($t = 0$). The time of flight of the atoms through the laser spot (250 ps) is much shorter than the pulse duration, hence the evolution of the pulse envelope during the time propagation of the Hamiltonian can be assumed negligible, that is, $g(t_p + t) \sim g(t_p)$. Since the effective Hamiltonian $H_{\text{eff}}(t)$ depends on the instantaneous intensity, it and thus $P_{\text{He}^+}(x,t_p)$ depend parametrically on x and t_p.

To reproduce the experimental ionization spectra, a large number of propagations must be performed for different values of x and t_p, taking into account the following experimental conditions:

(1) The incoming He$^-$ beam has a 1 mm diameter, which is much larger than the laser waist. The modeled ion signal must be averaged over the atomic beam cross section.

(2) The signal must be time integrated over the pulse duration.

(3) The photodetachment of He$^-$, producing neutral helium in the excited $1s2p\ ^3P^o$ state, is not uniform across the beam cross section. Therefore the distribution of neutral helium is not uniform either.

The above considerations lead to the following expression for the simulated ionization yield N:

$$N = \int_{\Delta t} dt_p \int_0^R dx \; w(x) \, P_{\text{He}^+}(x,t_p) \, P_{\text{He}}(x,t_p) \, \Phi_{\text{He}^-}, \qquad (25)$$

where Δt is the pulse duration, R the atomic beam radius, P_{He^+} the probability to ionize neutral helium, P_{He} the probability to photodetach He$^-$ in the $1s2p\ ^3P^o$ channel, and Φ_{He^-}

the incoming He$^-$ flux; $w(x)$ is the weight associated with the position x in the atomic beam, obtained from simple geometrical considerations:

$$w(x) = 4\sqrt{R^2 - x^2}. \tag{26}$$

The ω dependence of N, P_{He^+}, and P_{He} has been omitted from the notation for clarity.

For a Gaussian pulse, the photodetachment probability P_{He} is given by

$$P_{\mathrm{He}}(x,t_p) = 1 - \exp\left(-\frac{I(0;x,t_p)}{\omega}\sqrt{\frac{\pi}{2}}\frac{w_0}{v_{\mathrm{He}}}\sigma(\omega)\right), \tag{27}$$

where $I(0;x,t_p)/\omega$ is the photon flux, $\sqrt{\frac{\pi}{2}}w_0/v_{\mathrm{He}}$ the interaction time, and $\sigma(\omega)$ the ω-dependent photodetachment cross section. In the calculations reported here, we use the values of the cross section calculated by Ramsbottom and Bell [37], giving, e.g., $\sigma \simeq 10.6$ Mb for $\omega = 0.0646$ a.u. ($\lambda = 705$ nm).

Detachment and ionization have been treated so far as independent rather than sequential events. A model taking into account their sequential nature requires an additional integration of the ionization probability over the propagation time delayed by the photodetachment event, weighted by the instantaneous photodetachment yield. This is yet to be fully implemented in our model, although preliminary calculations show that it affects only a small range of frequencies close to the $1s2p$-$1s3s$ resonance, where the $1s3s$ ^3S state may be populated even at low intensities.

V. RESULTS

Diagonalizing the effective Hamiltonian gives a set of complex quasienergies E of the form

$$E = E_0 + \Delta E - i\frac{\Gamma}{2}, \tag{28}$$

where $E_0 + \Delta E$ is the Stark-shifted energy of the dressed atomic state and Γ its total ionization rate. In order to assess our choice of model space and to validate the associated computer code, we first performed a comparison of the quasienergies obtained using the model with those obtained from RMF calculations. The agreement was satisfactory, indicating that the main physical properties of the ionization process are accounted for.

We now consider the field-dressed atomic states used for the modeling of the experiment. They can be identified by plotting the real part of the quasienergies as a function of the photon energy ω as in Figs. 5 and 6. The dashed curves correspond to the field-free energy of the $1s2p$ state and of the $1s3s$ state shifted down by one photon energy, while the full curves are the results of the EH calculation. For the case $M_L = \pm1$ at an intensity of 3.6×10^{10} W/cm^2, the $1snp$ and $1snf$ Rydberg states can be populated by a two-photon transition from the initial $1s2p$ $^3P^o(M_L = \pm1)$ state, and are represented by the lines of slope -2ω. The value of n can be determined by extrapolating the lines to $\omega = 0$. The thick dot-dashed line indicates the two-photon ionization threshold. The horizontal line is the energy of the initial dressed $1s2p$ $^3P^o(M_L = \pm1)$ state, Stark shifted down compared to its field-free value. The Stark shift of the Rydberg states is extremely small, of the order of 5×10^{-5} a.u.

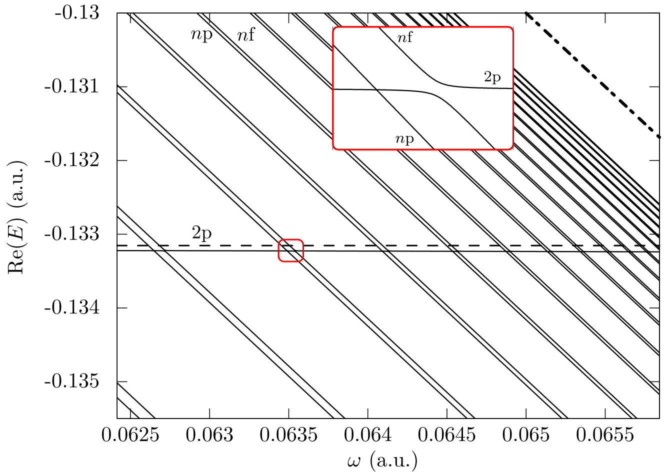

FIG. 5. (Color online) Real part of the EH quasienergies for $M_L = \pm1$ as a function of the laser angular frequency at a fixed intensity of 3.6×10^{10} W/cm^2. For each pair of Rydberg states, the lower line corresponds to $1snp$, and the upper line to $1snf$, with $6 \leqslant n \leqslant 22$. The horizontal dashed line corresponds to the field-free energy of the $1s2p$ state. The thick dot-dashed line in the upper right corner is the two-photon ionization threshold. The inset is a magnified view of the crossing highlighted in the small box.

At resonance, i.e., when $E_{2p} + 2\omega = E_{n\ell}$, the diabatic dressed-state energies intersect. The adiabatic energies exhibit avoided crossings whose distance of closest approach is proportional to the strength of the interaction between the states. The coupling of the initial state with the $1snf$ Rydberg states is stronger than with $1snp$ states. This implies that multiphoton ionization proceeds preferentially through the $(2 + 1)$

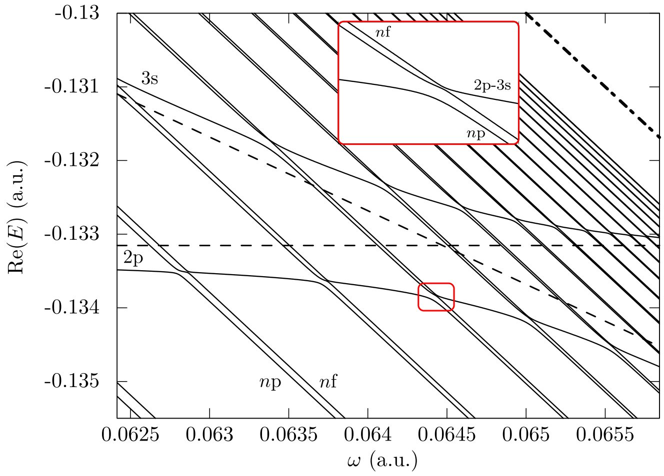

FIG. 6. (Color online) Real part of the EH quasienergies for $M_L = 0$ as a function of the laser angular frequency at a fixed intensity of 3.6×10^{10} W/cm^2. For each pair of Rydberg states, the lower line corresponds to $1snp$, and the upper line to $1snf$, with $6 \leqslant n \leqslant 22$. The horizontal dashed line corresponds to the field-free energy of the $1s2p$ state, while the oblique dashed line corresponds to the energy of the $1s3s$ state shifted down by ω. The thick dot-dashed line in the upper right corner is the two-photon ionization threshold. The inset is a magnified view of the crossing highlighted in the small box.

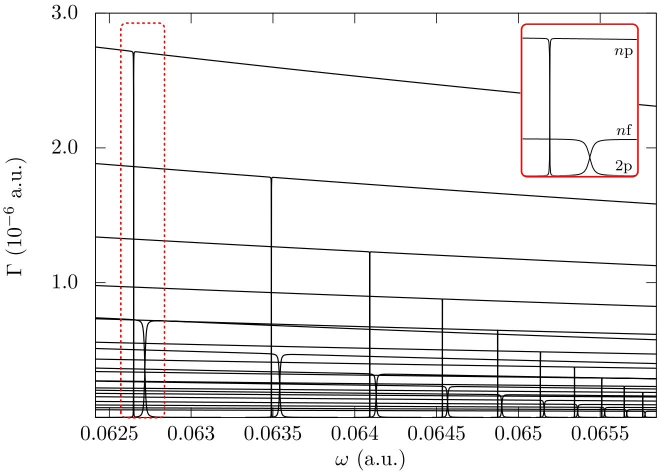

FIG. 7. (Color online) Total ionization rates for $M_L = \pm 1$, for $n = 7$ up to $n = 16$, as a function of the laser angular frequency at a fixed intensity of 3.6×10^{10} W/cm^2. The inset is a magnified view of the narrow region highlighted by the box.

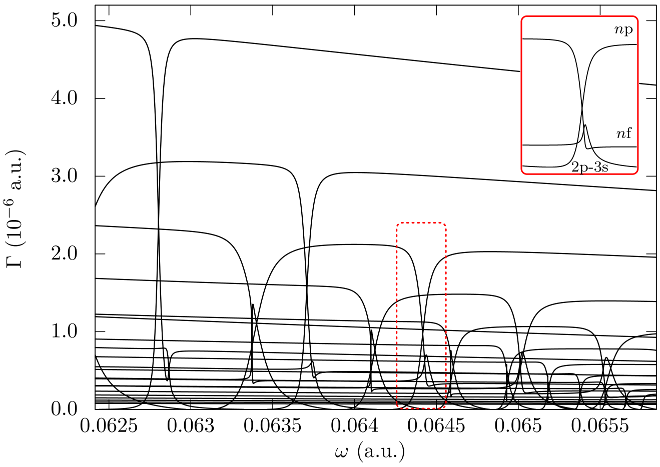

FIG. 8. (Color online) Total ionization rates for $M_L = 0$, for $n = 7$ up to $n = 16$, as a function of the laser angular frequency at a fixed intensity of 3.6×10^{10} W/cm^2. The inset is a magnified view of the narrow region highlighted by the box.

REMPI scheme into the $1snf$ states, followed by one-photon ionization into the $\ell = 2$ and $\ell = 4$ continua. Branching ratios calculated using the RMF and QDT approaches indicate a propensity (∼97%) for the photolectron to be ejected in the $\ell = 4$ channel.

For the case $M_L = 0$, shown in Fig. 6, the dressed-state energies exhibit a much richer structure. In addition to the initial state and the two Rydberg series, resonances with the $1s3s\ ^3S$ state are also present. The initial $1s2p\ ^3P^o(M_L = 0)$ state interacts strongly with the $1s3s\ ^3S$ state resulting in a very large avoided crossing centered around $\omega_r = 0.064\,47$ a.u. and extending over a broad range of photon energy. As the $1s3s\ ^3S$ state is populated by absorption of one photon, its energy curve has a slope of $-\omega$ away from the crossing. The presence of this physical intermediate state implies that the ionization preferentially occurs following a (1 + 1 + 1) REMPI scheme, via the $1snp$ Rydberg states. Branching ratios obtained from our RMF and QDT calculations indicate a 30% probability for the photoelectron to be ejected in the $\ell = 0$ channel and a 70% probability to be in the $\ell = 2$ channel.

One further consequence of the strong interaction between the $1s2p\ ^3P^o$ and $1s3s\ ^3S$ states is that the Stark shift of the $1s2p\ ^3P^o(M_L = 0)$ state is of opposite sign on either side of the resonance: Below the resonance, the energy is shifted down, while above the resonance it is shifted up. A manifestation of this difference will be seen in the ionization spectra presented below.

The ionization rates, related to the imaginary part of the quasienergies by (28), are plotted in Fig. 7 as a function of the photon energy ω for $M_L = \pm 1$. The plateaus correspond to the one-photon ionization rates of the Rydberg states, while the nonresonant three-photon ionization rate of the $1s2p\ ^3P^o(M_L = \pm 1)$ initial state is about three or four orders of magnitude smaller. In the region of two-photon resonances between the initial and the Rydberg states, the ionization rates cross over a range of ω whose width characterizes the interaction strength. The one-photon ionization rate of the $1snf$ is lower than that of $1snp$ due to the centrifugal barrier, but the two-photon $1s2p$–$1snf$ interaction is stronger than the $1s2p$–$1snp$ interaction.

Ionization rates for $M_L = 0$, shown in Fig. 8, present plateaus corresponding to the Rydberg states, while the $1s2p\ ^3P^o(M_L = 0)$ and $1s3s\ ^3S$ ionization rates are negligible on the scale of the figure. The presence of the $1s3s\ ^3S$ state again significantly enriches the picture: The number of resonances is increased and the strong one-photon interaction with the $1s2p\ ^3P^o(M_L = 0)$ initial state broadens the range of ω over which the crossings occur. EH calculations show that the asymmetry of the crossings is due to two-photon couplings between Rydberg states via the continuum.

The dynamical counterpart of the time-independent results presented so far is embodied in the simulated ionization yield which is obtained by propagating the wave function in time according to the scheme (21). As an example, the simulated ionization yield computed for a pulse energy of 6 mJ is plotted in Fig. 9, while the corresponding experimental ionization yield is shown in Fig. 10. The simulated spectrum is the sum of the computed yields for $M_L = 0$ and $M_L = \pm 1$, weighted by their initial populations resulting from the double capture process followed by the photodetachment of He$^-$. These populations are not accurately known but can be estimated using the β factor for the photodetachment of He$^-(^4P^o)$, which is 1.52 at about 700 nm [38]. This indicates that the ejected electron is strongly polarized and hence the remaining neutral helium is unpolarized. Consequently, the population is equally distributed among states parallel ($M_L = \pm 1$) and perpendicular ($M_L = 0$) to the laser field. We indeed found that the best fit to the experimental spectrum is obtained when we assume that 50% of the atoms are in the $M_L = 0$ state with the rest in the $M_L = \pm 1$ states. We therefore use this distribution in what follows.

In both spectra, a series of double peaks is visible: The peak at lower ω corresponds to a (1 + 1 + 1) REMPI process via the $1snp$ state, which is favorable for $M_L = 0$; the peak at higher ω corresponds to a (2 + 1) REMPI process via the Rydberg $1snf$ state, favorable for $M_L = \pm 1$. It should be noted

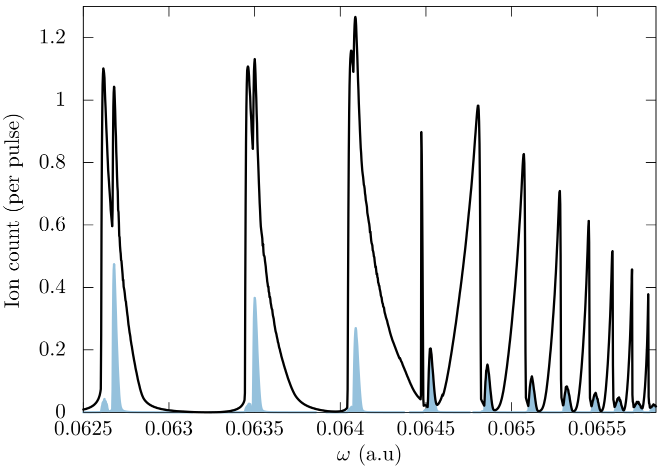

FIG. 9. (Color online) Simulated ionization spectrum for a laser pulse energy of 6 mJ. The shaded curve is the contribution from $M_L = \pm1$ states and the full line is the weighted sum of the contributions from $M_L = 0$ and $M_L = \pm1$ states.

that the assignment of the peaks corresponds to their major contributors: It is of course possible to ionize, for example, via a $1snf$ Rydberg state for $M_L = 0$, albeit with a small probability.

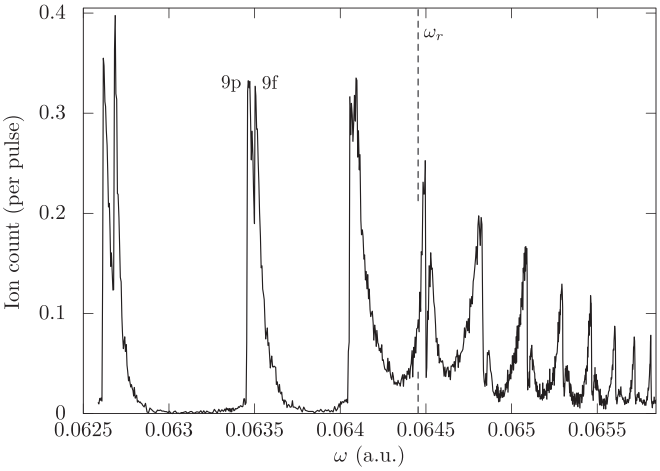

FIG. 10. Experimental ionization spectrum for a laser pulse energy of 6 mJ. The vertical dashed line indicates the $1s2p$-$1s3s$ resonance frequency ω_r.

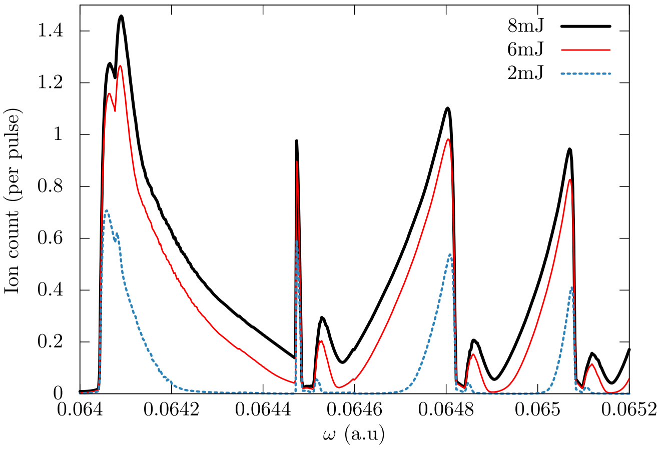

FIG. 11. (Color online) Simulated ionization spectra for 8, 6, and 2 mJ laser pulses.

The precise position of each resonance depends on the laser intensity which influences the Stark shift of the initial $1s2p\ {}^3P^o$ and the intermediate $1s3s\ {}^3S$ states, while that of the Rydberg states is very small. The peaks are asymmetric with the sharp rise corresponding to zero-field resonances between the $1s2p\ {}^3P^o$ and Rydberg states. In this case, transfer of population occurs early in the propagation through the laser field, maximising the interaction time and the probability of ionization. Above the zero-field resonance and for $M_L = \pm1$, the atom needs to experience a field strong enough to induce a downward Stark shift to bring it into resonance with a Rydberg state. This effect will extend over a wider range of frequencies as the pulse energy increases. Since the laser beam profile is Gaussian, the Stark-induced resonance will occur twice, during the onset and the falloff of the laser intensity experienced by the atom, whose population is transferred back to the initial state by adiabatic rapid passage [29]. The ionization yield is smaller since the interaction of the Rydberg state with the laser field is greatly reduced, explaining the tail of the peaks towards higher frequencies as a result of this dynamic blueshift. For $M_L = 0$, the physics is more complicated due to the existence of the one-photon resonance with the $1s3s\ {}^3S$ state at $\omega_r = 0.064\,47$ a.u. As illustrated by the two-state model in Sec. III A, for $\omega < \omega_r$, the Stark shift of the initial state leads to resonances with Rydberg states at lower photon energies, while the inverse is true for $\omega > \omega_r$, leading to a dynamic redshift. Hence the asymmetry of the peaks in the ionization yield is reversed as the $1s2p$-$1s3s$ resonance is crossed. The two successive one-photon transitions lead to more complex population dynamics, resulting in an ionization yield larger than for $M_L = \pm1$. This is clear from the comparison between the total spectrum and the separate spectrum for $M_L = \pm1$ presented in Fig. 9.

Although the simulated and experimental spectra presented in Figs. 9 and 10 are qualitatively similar, there are discrepancies in the magnitudes of the ion yields, with the simulated values larger than the measurements by a factor between 3 and 4. This may be due to detection inefficiency in the experiment or an overestimation of the initial population of the He($1s2p\ {}^3P^o\ M_L = 0,\pm1$) states in the numerical simulation. To improve estimates of the detailed initial population would require more experimental and theoretical work, starting from charge exchange of He$^+$ and He on cesium and involving a full time-dependent three-electron model for photodetachment of He$^-({}^4P^o_J)$. The larger simulated ion yields may also be due to imprecisions in some couplings in our semiperturbative EH model; for instance, those involving the continuum which are not possible to validate *ab initio*. Furthermore, the heights of the measured peaks decrease rapidly with increasing ω, which is not reproduced to the same extent in our model. These discrepancies remain to be explained.

Figures 11 and 12 show the variation of the ionization yield with respect to the pulse energy, which determines the peak laser intensity experienced by the atoms. As one would

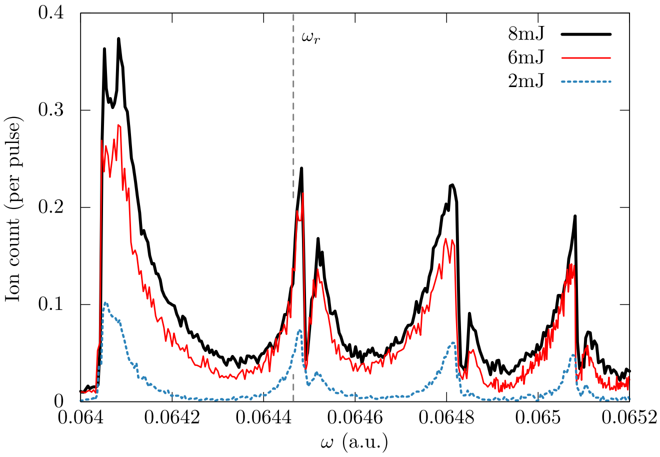

FIG. 12. (Color online) Experimental ionization spectra for 8, 6, and 2 mJ laser pulses. The vertical dashed line indicates the $1s2p$-$1s3s$ resonance frequency ω_r.

expect, the amplitude of the ion signal increases with the pulse energy, a consequence of the increased ionization probability and interaction volume. The tail of the peaks is broadened since the Stark shift of the $1s2p\ ^3P^o(M_L = 0)$ initial state is larger. A thorough analysis of the pulse energy dependence of the ion signal reveals no simple scaling, illustrating the complex interplay between the $(1+1+1)$ REMPI and $(2+1)$ REMPI mechanisms. We remark that the tails of the peaks in the simulation do not decay as rapidly as in the experiment, particularly for the highest pulse energy of 8 mJ. Their shape depends on the intensity of the field experienced by the atoms as they traverse the laser beam. A more accurate knowledge and control of the laser pulses is therefore essential in order to improve the simulation.

VI. CONCLUSION

We have reported a joint experimental-theoretical study of resonance-enhanced three-photon ionization of the $1s2p\ ^3P^o$ state of helium, for laser wavelengths in the range 690–730 nm coupling the initial state to $1snp$ and $1snf$ Rydberg states via a two-photon transition, for a number of pulse energies. The experiment is made possible by the development of a technique for producing a triplet-selective beam of excited $1s2p\ ^3P^o$ and $1s2s\ ^3S$ atoms from negative helium ions formed via a double capture process. The theoretical study is based on an effective Hamiltonian model reproducing the essential physical processes and trends seen in the experimental data. In particular, we have been able to distinguish two dynamical processes, depending on the value of the magnetic quantum number M_L of the initial $1s2p\ ^3P^o$ state. For $M_L = 0$, the dominant ionization path follows a $(1+1+1)$ REMPI mechanism via the $1s3s$ and $1snp$ Rydberg states. For $M_L = \pm 1$, no intermediate one-photon resonance exists and the ionization process follows a $(2+1)$ REMPI mechanism involving a two-photon transition into a $1snp$ or $1snf$ Rydberg state, with a propensity for populating the latter. The precise position of these one- and two-photon resonances depends on the relative Stark shifts of the dressed atomic states, which in turn depends on the intensity of the laser field experienced by the atom. These shifts give rise to asymmetric peaks in the experimental ionization spectrum, reflecting the intensity profile of the laser pulse. The slow falloff in the ionization yield is reproduced reasonably well by our model, in particular, its broadening with increasing pulse energy and its reversal for $M_L = 0$ as the laser frequency crosses the $1s2p\ ^3P^o$–$1s3s\ ^3S$ resonance at $\omega_r = 0.064\,47$ a.u. ($\lambda = 706.7$ nm). The latter behavior is due to the large avoided crossing between the dressed $1s2p\ ^3P^o$ and $1s3s\ ^3S$ states, as predicted by a simple two-state model. Discrepancies remain between the model and the experiment, but overall the good qualitative agreement gives us confidence that the major mechanisms at play in the three-photon ionization process have been elucidated.

As it stands, the model treats the photodetachment of He$^-$ and the multiphoton ionization of He as independent events. In a small region around the $1s2p\ ^3P^o$–$1s3s\ ^3S$ resonance, the numerical simulation shows an onset of MPI before the rise of the photodetachment probability of He$^-$. It should also be noted that in this resonance region the photodetachment process leaves the helium atom not in the field-free $1s2p$ state but in a strong mixture of the $1s2p$ and $1s3s$ states. A consistent treatment of photodetachment and multiphoton ionization of the resulting dressed state is a perspective for future work.

The photodetachment of He$^-$ may also leave the helium atom in the $1s2s\ ^3S$ state. The mechanisms of three-photon ionization of this state are nearly identical to the $M_L = \pm 1$ case, and can thus be studied using a similar approach. Ionization would, in this case, proceed through Rydberg $1sns$ and $1snd$ states, in contrast with the $1snp$ and $1snf$ states appearing in the present work. Another field of interest is the multiphoton ionization of excited helium under circularly polarized light. The different selection rules implied are expected to modify the population of the different ionization channels, highlighting anew the role of the magnetic quantum number M_L. In this respect, a proper modeling of the M_L population created by the initial photodetachment is needed. The ionization of the $1s2p\ ^3P^o$ and $1s2s\ ^3S$ states under circular polarization, along with the ionization of $1s2s\ ^3S$ by a linearly polarized laser field, will be the subject of a forthcoming paper.

ACKNOWLEDGMENTS

This work has been supported by the Fund for Scientific Research-FNRS through IISN Contract No. 4.4504.10. Computational resources have been provided by the Université catholique de Louvain (CISM/UCL) and the Consortium des Équipements de Calcul Intensif en Fédération Wallonie Bruxelles (CÉCI) funded by the F.R.S.-FNRS under Contract No. 2.5020.11, as well as by the Institut de Physique de Rennes. We also thank Bernard Piraux for useful discussions.

---

[1] J. A. R. Samson, Z. X. He, L. Yin, and G. N. Haddad, J. Phys. B: At. Mol. Opt. Phys. **27**, 887 (1994).

[2] J. S. Briggs and V. Schmidt, J. Phys. B: At. Mol. Opt. Phys. **33**, R1 (2000).

[3] C. J. Joachain, N. J. Kylstra, and R. M. Potvliege, *Atoms in Intense Laser Fields* (Cambridge University Press, Cambridge, UK, 2012).

[4] M. K. Odling-Smee, E. Sokell, P. Hammond, and M. A. MacDonald, Phys. Rev. Lett. **84**, 2598 (2000).

[5] R. F. Stebbings, F. B. Dunning, F. K. Tittel, and R. D. Rundel, Phys. Rev. Lett. **30**, 815 (1973).

[6] A. Burgess and M. J. Seaton, Mon. Not. R. Astron. Soc. **120**, 121 (1960).

[7] V. Jacobs, Phys. Rev. A **3**, 289 (1971).

[8] M. Gisselbrecht, D. Descamps, C. Lyngå, A. L'Huillier, C.-G. Wahlström, and M. Meyer, Phys. Rev. Lett. **82**, 4607 (1999).

[9] T. N. Chang and M. Zhen, Phys. Rev. A **47**, 4849 (1993).

[10] T. N. Chang and T. K. Fang, Phys. Rev. A **52**, 2638 (1995).

[11] F. B. Dunning and R. F. Stebbings, Phys. Rev. Lett. **32**, 1286 (1974).

[12] L.-A. Lompré, G. Mainfray, B. Mathieu, G. Watel, M. Aymar, and M. Crance, J. Phys. B: At. Mol. Phys. **13**, 1799 (1980).

[13] H. Haberland, M. Oschwald, and J. T. Broad, J. Phys. B: At. Mol. Phys. **20**, 3367 (1987).

[14] M. Madine and H. van der Hart, J. Phys. B: At. Mol. Opt. Phys. **38**, 3963 (2005).

[15] M. Madine and H. van der Hart, J. Phys. B: At. Mol. Opt. Phys. **39**, 4049 (2006).

[16] S. Hussain, M. Saleem, M. Rafiq, and M. A. Baig, Phys. Rev. A **74**, 022715 (2006).

[17] P. Reinhed, A. Orbán, J. Werner, S. Rosén, R. Thomas, I. Kashperka, H. Johansson, D. Misra, L. Brännholm, M. Björkhage *et al.*, Phys. Rev. Lett. **103**, 213002 (2009).

[18] U. V. Pedersen, M. Hyde, S. P. Møller, and T. Andersen, Phys. Rev. A **64**, 012503 (2001).

[19] H. D. Zeman, Rev. Sci. Instrum. **48**, 1079 (1977).

[20] P. G. Burke, P. Francken, and C. J. Joachain, J. Phys. B: At. Mol. Opt. Phys. **24**, 761 (1991).

[21] M. Dörr, M. Terao-Dunseath, J. Purvis, C. J. Noble, P. G. Burke, and C. J. Joachain, J. Phys. B: At. Mol. Opt. Phys. **25**, 2809 (1992).

[22] P. G. Burke, *R-Matrix Theory of Atomic Collisions: Application to Atomic, Molecular and Optical Processes* (Springer-Verlag, Berlin, 2011).

[23] H. C. Baker, Phys. Rev. A **30**, 773 (1984).

[24] J. P. Killingbeck and G. Jolicard, J. Phys. A: Math. Gen. **36**, R105 (2003).

[25] G. Jolicard and J. P. Killingbeck, J. Phys. A: Math. Gen. **36**, R411 (2003).

[26] NIST Atomic Spectra Database, http://www.nist.gov/pml/data/asd.cfm

[27] *Springer Handbook of Atomic, Molecular, and Optical Physics*, edited by G. W. F. Drake (Springer-Verlag, New York, 2006), Vol. 1.

[28] P. Durand, Phys. Rev. A **28**, 3184 (1983).

[29] B. W. Shore, *The Theory of Coherent Atomic Excitation: Multilevel Atoms and Incoherence* (Wiley, New York, 1990), Vol. 2.

[30] K. M. Dunseath, J.-M. Launay, M. Terao-Dunseath, and L. Mouret, J. Phys. B: At. Mol. Opt. Phys. **35**, 3539 (2002).

[31] M. J. Seaton, Rep. Prog. Phys. **46**, 167 (1983).

[32] DLMF, NIST digital library of mathematical functions, http://dlmf.nist.gov/33.14, release 1.0.6 of 2013-05-06.

[33] A. R. Barnett, Comput. Phys. Commun. **27**, 147 (1982).

[34] C. J. Noble, Comput. Phys. Commun. **159**, 55 (2004).

[35] R. Piessens, E. de Doncker-Kapenga, C. W. Überhuber, and D. K. Kahaner, *QUADPACK: A Subroutine Package for Automatic Integration, Springer Series in Computational Mathematics* (Springer-Verlag, Berlin, 1983).

[36] R. B. Sidje, ACM Trans. Math. Soft. (TOMS) **24**, 130 (1998).

[37] C. A. Ramsbottom and K. L. Bell, J. Phys. B: At. Mol. Opt. Phys. **32**, 1315 (1999).

[38] D. J. Pegg, J. S. Thompson, J. Dellwo, R. N. Compton, and G. D. Alton, Phys. Rev. Lett. **64**, 278 (1990).